Journal Name

Large-scale Atomistic Simulations of Lithium Diffusion in a Graphite Anode with a Machine Learning Force Field[†]

Jianli Cheng,[*a] James M. Stevenson[a], Garvit Agarwal[a], John L. Weber[a], Leif D. Jacobson[a] and Karl Leswing[a]

Graphite is the anode material in the vast majority of current commercial lithium-ion batteries (LIBs) due to its excellent electrochemical performance and abundant reserves. However, the development of high-performance LIBs still faces technical bottlenecks including limited rate capability, partly because of the slow Li diffusion in the graphite anode. Experimental measurements of Li diffusivity versus Li contents in graphite show both monotonic and non-monotonic trends with reported Li diffusivity spanning orders of magnitude. Comprehensive insights of the Li diffusion process and its bottleneck in graphite are essential to develop the next-generation LIBs. In this work, we developed a machine learning force field (MLFF) to investigate the Li diffusion in the Li_xC_6 system. We benchmark density functional theory (DFT) functionals and dispersion corrections versus experiment, finding nonlocal van der Waals functional rVV10 shows a good agreement with experimental results in terms of the structural, energetic, and electrochemical properties of the Li_xC_6 system. We then train a MLFF based on our recently developed charge recursive neural network (QRNN) architecture to simulate Li diffusion in graphite at different Li contents, stage structures and temperatures. Our Li diffusion analysis demonstrates a phase-transition dependent Li diffusion in the Li_xC_6 system, which supports the experimental measurements of a non-monotonic relation between Li diffusivity and Li content. This work demonstrates the capability of our QRNN model in carrying out large scale molecular dynamics simulations to identify the Li diffusion bottleneck in a graphite anode.

1 INTRODUCTION

Since the commercialization of rechargeable lithium-ion batteries (LIBs) in 1991, they have become the ubiquitous power sources for portable electronic devices, electric vehicles, and grid electricity storage. Over the past three decades, extensive research efforts have been invested to develop new generations of cathode and anode materials with enhanced cycling performance. Nonetheless, graphite is still the dominant anode for commercial LIBs because of its superior reversibility of Li de-/intercalation and low cost.[1,2] Graphite is a layered material consisting of graphene sheets, which have strong covalently bonded carbon atoms forming a network of honeycombs in each layer. The binding forces between each layer arise from weak dispersion or van der Waals (vdW) interactions, enabling the intercalation of ionic and molecular species. Upon Li intercalation, the vdW interactions are screened, and the graphene layers glide with respect to each other, resulting in a symmetry change from an AB stacking (see Figure 1b) in graphite (C_6) to an AA stacking (see Figure

1d) in the fully lithiated state (LiC_6).[3] In addition, the Li de-/intercalation within graphite follows a concentration-dependent staging mechanism, where stage n contains n graphene layers between two intercalated Li layers. For example, LiC_{12} is a stage 2 compound with two graphene layers between two Li layers. The first model to explain the staging mechanism was proposed by Rudorff and Hofmann.[4] However, their model fails to explain the phase transition between stage 2 and stage 3 Li_xC_6 structures. An improved model by Daumas and Herold[5] was then introduced to explain the phase transitions between the stages, where the graphene layers could be elastically bent and deformed around domains of the intercalated species.[2] Despite various computational simulations[3,6] and experimental characterizations[7,8], the staging mechanism is not yet fully understood. In addition, the phase transitions during Li de-/intercalation within graphite impacts Li diffusion.[9] It has been reported that the transitions towards the densely lithiated stages 1 and 2 contribute to the rate limitations for charge and discharge due to the sluggish Li diffusion.[10] On the other hand, the experimentally measured Li diffusion coefficients in graphite have been reported with a very wide range of values, from 10^{-6} to 10^{-16} cm^2,[11–14] depending on the electrical potentials, the experimental methodology, and the elec-

trochemical systems.

Contradicting conclusions have been reported regarding the change of Li diffusivity as a function of Li concentration. For example, using the galvanostatic intermittent titration Technique (GITT) Park et al.[15] found a phase transition dependent Li diffusivity versus Li content and an overall increasing Li diffusivity with a higher Li content in Li_xC_6 while Piao et al.[16] showed a monotonic relation between Li diffusivity versus Li content and a decreasing Li diffusivity with a higher Li content using AC impedance measurements. Computational simulations have also been implemented to calculate Li diffusion coefficients in graphite. Using first-principles calculations combined with Monte Carlo simulations, Persson et al. reported a high Li diffusivity of 10^{-7} to 10^{-6} cm^2/s in the direction parallel to the graphene layers.[3,17] In their calculations, the interlayer spacing between empty graphene layers was fixed during simulations while experimentally, the layer spacing increases with a higher Li content.[11] In addition, only stage 1 and 2 structures are considered and Li diffusivity was calculated for $x > 0.2$ in Li_xC_6.[3,17]

In this study, we investigate the phase transitions and Li diffusion in the Li_xC_6 system as a function of stage structure, Li content, and temperature. Given the high computational cost of *ab initio* molecular dynamics due to the large size and time scales required to obtain sufficient diffusion statistics, especially at low temperatures, we train a machine learning force field (MLFF) based on our recently reported charge recursive neural network architecture (QRNN)[18] for simulating the Li diffusion in the Li_xC_6 system with $0 \leq x \leq 1$ and stage 1, 2, 3, 4, and 1L. Our QRNN model was trained with a dataset labeled by density functional theory (DFT) calculations with the nonlocal van der Waals functional rVV10. We demonstrate that comparing with the PBE functionals and previously reported *ab initio* results, the rVV10 functional accurately reproduces the experimental lattice parameters, phase stability, and voltage profile of the Li_xC_6 system. Previously, we developed a QRNN model trained to non-periodic DFT data for liquid electrolyte simulations and our predicted bulk thermodynamic and transport properties of pure carbonate solvents and electrolyte mixtures agree well with experimental results.[19] In this work, we demonstrate that our QRNN architecture also works well for periodic systems. Our QRNN model is accurate and stable, allowing us to perform large scale molecule dynamics simulations to explore Li intercalation and diffusion in the graphite anode.

2 Computational Details and Structural Modeling

2.1 DFT calculations

All the density functional theory (DFT) electronic structure calculations were performed using the Quantum Espresso (QE) software package[20] with the Ultrasoft (US) pseudopotentials (PPs).[21] The wavefunction and charge density cutoffs were set to 40 Ry and 200 Ry, respectively. Cell parameters and atomic positions were relaxed with a threshold of 10^{-3} Ry/Bohr for the atomic forces and 10^{-5} Ry/Bohr for the energies. The Monkhorst–Pack method was used to sample the k-points in the Brillouin zone with a k-mesh sampling density greater than
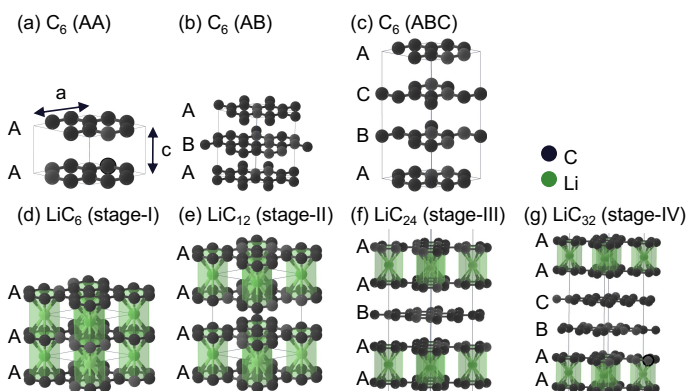

Fig. 1 The schematic figures to show the structures of Li_xC_6 compounds at different stages. The Li-graphite structures in d-g were used to sample different Li-vacancy arrangements.

15,625 points per $Å^3$. As the standard DFT lacks the description of the vdW interactions[22], we benchmarked three approaches to include vdW interactions: PBE-D3, PBE D3-BJ, and rVV10, and we selected the functional by comparing the DFT calculated lattice parameters, thermodynamic stability, and voltage profile of the Li_xC_6 compounds with the experimental results. The thermodynamic stability of Li_xC_6 compounds at different Li concentrations (x) and stages was evaluated by calculating the formation energies (E_f) with respect to C_6 and LiC_6:

$$E_f = E(Li_xC_6) - xE(LiC_6) - (1-x)E(C_6) \quad (1)$$

where E is the calculated total energy of the Li_xC_6 compound at different Li concentrations. With the calculated E values, the voltage profile at 0 K for the Li_xC_6 system as a function of Li content can be calculated as:

$$V_x = \frac{E(Li_{x_2}C_6) - E(Li_{x_1}C_6) + (x_1 - x_2)E(Li)}{(x_1 - x_2)e} \quad (2)$$

2.2 Structure and training dataset construction

For each stage of Li_xC_6 compound, we sampled different Li-vacancy arrangements in Li_xC_6 with a total of 1254 structures, and then we calculated the energy and force for each relaxed structure using the rVV10 functional. Figure 1 illustrates the structures of the stage 1, 2, 3, and 4 Li_xC_6 compounds for sampling different Li-vacancy arrangements. In addition, we added 26 structures from four Li diffusion pathways (see Figure 4) to construct an initial dataset of 1280 structures. These four diffusion pathways include Li diffusion with two neighboring Li (Pathway 1), with one neighboring Li (Pathway 2), without neighboring Li (Pathway 3), and through a perfect carbon honeycomb (Pathway 4). The two end points of each diffusion pathway were fully relaxed, and the structures used to generate the diffusion pathways were stage 2 Li_xC_6 compounds. The transition-state search and energy barrier calculation for the Li diffusion processes were conducted with the climbing-image nudged elastic band (cNEB)[23] method as implemented in QE. The QRNN predicted transition-states and energy barriers were calculated by the *NEBOptimizer* in ASE with the QRNN model as the calculator.

Next, the atomic charges of each structure in the dataset were labeled with GFN1-xTB.[24] Using this dataset, we trained an initial QRNN model for carrying out active learning loops to sample additional Li_xC_6 structures. Each active learning round consists of model exploration, data labeling, QRNN model training, and model stability testing. In the exploration step, we carried out molecular dynamics (MD) simulations of the Li_xC_6 compounds with the Atomic Simulation Environment package (ASE)[25] using an intermediate trained QRNN model as the calculator. Please note that the ASE MD was only used for the sampling purpose, and the MD for diffusion calculations was carried out by Desmond (2024-3).[26] We performed ASE NPT MD at 300 and 6000 K for 10 ps using Li_xC_6 structures with the number of atoms less than 200. We sampled the structures from the MD trajectories of different stages of Li_xC_6 compounds to improve the model's generalizability on all Li_xC_6 compounds. In the labeling step, we carried out DFT calculations on the sampled structures to obtain energies and forces, which were added to the existing training dataset. A new QRNN model was then trained with the updated dateset and tested for model stability by running Desmond MD. We found that the model instability is mainly due to spurious graphite structural change from layered to disordered. Therefore, we ran ASE MD at 6000 K to sample the snapshots of the trajectory leading up to the structural change, labeled them with DFT, and added the data the training dataset. After three rounds of active learning, we were able to obtain a QRNN model that is stable for the Li_xC_6 system at different Li contents, stage structures and temperatures. In total, we have 3065 entries in the dataset.

2.3 Model training

We implemented our previously developed QRNN architecture[18] to train the Li_xC_6 model. Modified Behler and Parrinello symmetry functions[27] were used to compute an atomic environment vector (AEV) for each atom. The AEV describes both local geometric and charge environment, and is composed of radial and angular symmetry functions for atom i (G_i^{AEV}), charge-weighted radial AEV (G_i^{qR}), and atomic charge (q_i). The AEV is then used as an input into an atomic neural network that transforms the atomic AEV into an output E_i. The total energy E_T of the system is the sum over all i "atomic contribution", and is defined as:

$$E_T = \sum_i^{N_{atoms}} E_i(q_i, G_i^{qR}, G_i^{AEV}) + E_{disp} + E_{coul}(q) \quad (3)$$

where E_{disp} is the empirical D2 dispersion correction[28] and E_{coul} is a truncated Coulomb energy, which decays smoothly at short-range[18]. The forces can be expressed as the first derivative of E_T with respect to the atomic positions. To train a QRNN model, we used a training:validation split of 99:1 and a learning rate of 2×10^{-3}, and the optimized QRNN model was obtained by minimizing the loss functions of the predicted energies and forces with respect to the DFT training data.

2.4 Diffusivity calculations

In this study, we simulated Li intralayer diffusion in bulk graphite without any defects. To calculate the Li diffusivity, classical MD simulations for the Li_xC_6 compounds at different stages, Li contents and temperatures were performed using the trained QRNN model in the MD package Desmond (2024-3).[26] In this study, we considered four different stages of Li_xC_6 compounds with $n = 1$, 2, 4, and 1L. The Li diffusion in stage 3 structures were approximated by that of stage 4 structures, as Li-Li interactions in the Li_xC_6 system are well-represented by repulsive short-range pair interactions[3] and the interlayer Li-Li interactions are screened by layers of graphene, therefore we expect stage 3 structures exhibit similar Li diffusion with stage 4 structures. Stage 1L represents a dilute stage 1 at very low Li concentrations.[9] Large supercells with lattice parameters between 25 to 65 Å and number of atoms between 10890 and 12800 were used, depending on the Li_xC_6 compound. In total, we generated 23 Li_xC_6 structures, which are illustrated in Figure S2-5 for stage 1, 2, 4, and 1L Li_xC_6 compounds, respectively. Stage 1 $Li_{0.987}C_6$, stage 2 $Li_{0.493}C_6$, and stage 4 $Li_{0.247}C_6$ were generated by randomly placing 1.33%, 0.67%, and 0.33% of Li vacancies in LiC_6, LiC_{12}, and LiC_{24}, respectively. Except for stage 1L and the previous three structures, we only placed Li vacancies in one Li layer for the other 18 structures to approximate the presence of two-phase co-existence between different stages. For example, $Li_{0.82}C_6$ exhibits both stage 1 and 2 region in its structure. For each MD run, we set the time step to 2 fs, and dumped the trajectory every 1 ps. To equilibrate the structure at each temperature, we ran 1 ns MD simulation in the NPT ensemble, and then we averaged the density over the last 0.5 ns trajectory and selected the structure whose density was closest to the average as the equilibrated structure. We also checked the density convergence by running a 20 ns NPT MD simulation, and we found that the density was well converged after 0.5 ns (see Figure S6). To perform diffusion analysis, we ran MD simulations in NVT ensemble for 3 ns at high temperature conditions ($500 < T \leq 900$ K) and up to 70 ns at low temperature conditions ($300 \leq T \leq 500$ K). From the obtained MD trajectories, the self-diffusion coefficients (D) were estimated by a linear fitting of the mean squared displacement (MSD) of all Li ions over time using the Einstein relation:[29]

$$D = \frac{1}{2d} d\langle \Delta r^2 \rangle / dt \quad (4)$$

where t is the time, r is the ion position, $\langle \Delta r^2 \rangle$ is the MSD and $d = 2$, which indicates two-dimensional Li diffusion in the Li layers.

3 RESULTS AND DISCUSSION

3.1 DFT benchmarking

In Table 1, we list the calculated lattice parameters for C_6, LiC_{12}, and LiC_6 from PBE D3, PBE D3-BJ, and rVV10. For each compound, the calculated a lattice parameters with different DFT methods are similar with a difference less than 0.02 and they agree well with experimentally reported values.[30] The c lattice parameters, on the other hand, vary significantly, which indicates the importance of correcting the vdW forces between the

Table 1 Comparison of calculated and experimentally determined lattice parameters (a and c in Å).

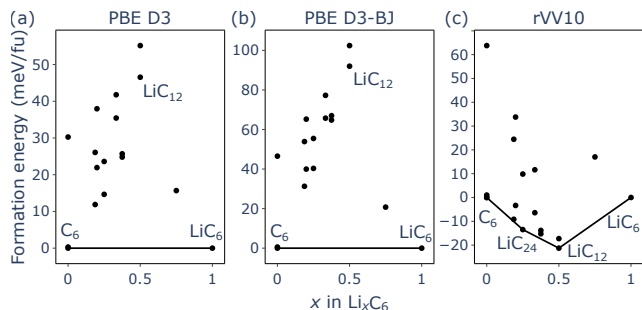| Composition	$a_{PBE\ D3}$	$a_{PBE\ D3-BJ}$	a_{rVV10}	a_{QRNN}	a_{exp}	$c_{PBE\ D3}$	$c_{PBE\ D3-BJ}$	c_{rVV10}	c_{QRNN}	c_{exp}
C_6	2.465	2.464	2.470	2.470	2.456[30]	6.969	6.750	6.679	6.701	6.700[30]
LiC_{12}	4.291	4.287	4.305	4.299	4.269[30]	7.134	6.988	6.962	6.925	7.023[30]
LiC_6	4.317	4.312	4.333	4.444	4.301[30]	3.636	3.592	3.623	3.686	3.687[30]

Fig. 2 Comparison of first-principles calculated formation energy per formula unit from (a) PBE D3, (b) PBE D3-BJ, and (c) rVV10. The solid lines in (c) indicate the convex hull.

graphene layers. Overall, we found that the best match with experimental lattice parameters[30] is obtained with the rVV10 functional. Next, we investigated the effect of DFT methods on thermodynamic stability of the Li_xC_6 compounds at different Li concentrations and stages. Here we considered four stages of Li_xC_6 with n=1, 2, 3, and 4. Figure 2 illustrates the calculated formation energies of 18 Li_xC_6 compounds from PBE D3, PBE D3-BJ, and rVV10. It can be seen that the formation energies of all intermediate Li_xC_6 compounds are above zero with PBE D3 and PBE D3-BJ, which indicates that the PBE functional tends to underestimate the thermodynamic stability of the Li_xC_6 compounds. On the other hand, the non-local rVV10 functional (see Figure 2c) predicts several stable intermediate Li_xC_6 compounds which lie on the convex hull, such as stage 2 LiC_{12} and stage 3 LiC_{24}. An earlier study reported that the stability underestimation from PBE D3 and PBE D3-BJ is mainly because the PBE functional overbinds the carbon atoms in C_6.[31] Using the PBE functional, Persson el al. had to add an empirical vdW binding energy for every empty graphite layer in stage 2 to properly study the thermodynamic and kinetic properties of the Li_xC_6 system.[3] Based on lattice parameters and thermodynamic stability results we selected the rVV10 functional for all following DFT calculations and constructing the training dataset.

3.2 QRNN validation

In Table 1, we list the QRNN calculated lattice parameters for C_6, LiC_{12}, and LiC_6. The lattice parameters from QRNN match well with both the results from the rVV10 functional and experiments, except the a lattice parameter of LiC_6, which exhibits an error of 0.143 . However, as Li intralayer diffusion barrier is more dependent on the c lattice parameter,[3] we do not expect the error on the a lattice parameter prediction greatly impacts intralayer Li diffusivity. As mentioned in Section 2, we sampled different Li-vacancy arrangements in stage 1, 2, 3, and 4 Li_xC_6 compounds to look for

ground state structures and construct the training dataset. Figure S1 shows the comparisons of the energies and forces calculated by QRNN and DFT on the training and validation datasets. The root mean squared error (RMSE) in energies are 1.689 meV/atom and 3.430 meV/atom for the training and validation datasets, respectively. The RMSE in forces are 0.94 eV/Å and 0.81 eV/Å for the training and validation datasets, respectively. Our energy and force RMSEs are comparable with recent MLFF models to study ionic diffusions.[32,33] Using the rVV10 functional, we calculated the formation energies of the sampled Li_xC_6 compounds and construct the convex hull in Figure 3a. We found that at x=0, C_6 with AB stacking is more stable than AA and ABC stacking; at x=0.5, stage-2 LiC_{12} with AA stacking is more stable than AB stacking; at x=1, stage-1 LiC_6 with AA stacking is more stable than AB stacking. The results are in agreement with previous theoretical and experimental results.[31,34] In addition, we found two ground state structures between $0 < x < 0.5$: LiC_{29} and LiC_{36}. Figure 3a also illustrates the formation energies and convex hull predicted by the QRNN model, which shows negative formation energies of some Li_xC_6 compounds and one intermediate ground state structure of a stage 2 LiC_{16}.

From the identified ground state structures on the convex hull, we calculated the voltage profile for the Li_xC_6 system as a function of Li content using Eqn. 2. Figure 3b shows the comparison between the experimental voltage profile of Li_xC_6[35] and the ones calculated by DFT and QRNN as well as a previously reported DFT result[3]. The tile lines in the convex hull plot represent the two-phase regions, which are illustrated by the plateaus of the voltage curves. It can be seen that our DFT calculated voltage profile has an excellent agreement with the experimental result and is more accurate than the previous DFT result, both in terms of the calculated voltage values and the phase transitions. While our QRNN-predicted voltage curve provides accurate voltage values, it only captures one phase transition, as QRNN predicts a single intermediate ground-state structure on the formation energy convex hull. It should be pointed out that a stage 2 LiC_{12} is only 3.98 meV per formula unit (fu) higher than the convex hull, which is within the formation energy RMSE at 5.69 meV/fu calculated by our QRNN model.

Figure 4a-c illustrate three Li diffusion pathways which represent the Li diffusion in different Li concentrations. Our DFT calculated Li diffusion barriers are 0.52 eV, 0.42 eV, and 0.43 eV for diffusion pathways with two neighboring Li (Pathway 1), one neighboring Li (Pathway 2) and no neighboring Li (Pathway 3), respectively (see Figure 4e-g). Figure 4d shows interlayer Li diffusion though a carbon hexagon (Pathway 4) with a diffusion barrier of 8.0 eV, which is more than one order of magnitude higher than the values of intralayer Li diffusion pathways. This indicates that
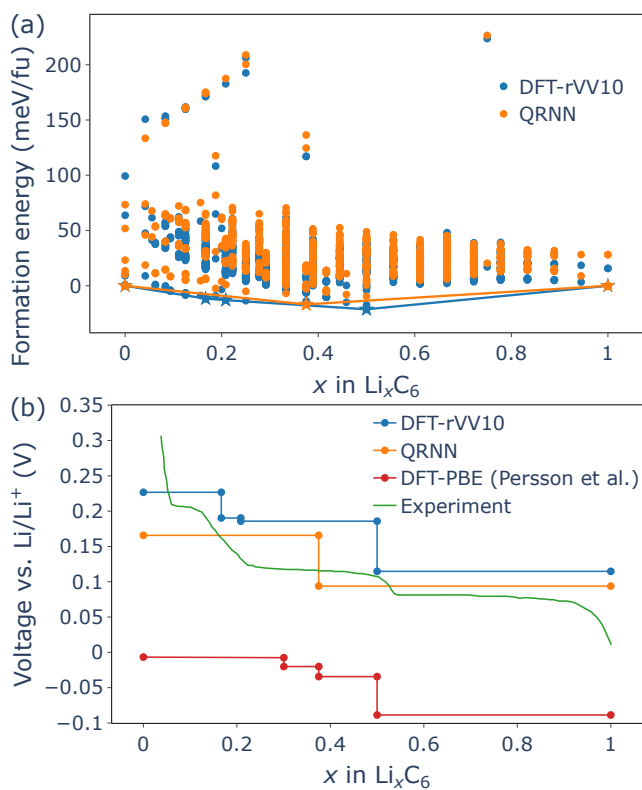
Fig. 3 (a) The formation energies of Li_xC_6 compounds at stage 1, 2, 3, and 4 calculated by DFT with rVV10 functional and QRNN model. The convex hull indicates the ground states which are connected by the solid lines. (b) The voltage profile for the Li_xC_6 system calculated by DFT and QRNN model. An experimental and a previously reported DFT voltage curves are plotted for comparison. [3,35]

Li diffusion in pristine graphite is restricted to two-dimensional intralayer diffusion. Our calculated diffusion barriers are in good agreement with previously reported values calculated by PBE D3-BJ. [36] The higher diffusion barrier in Pathway 1 is due to the repulsive short-range Li-Li interactions, which reduces Li mobility at a higher Li content. [3] The QRNN calculated diffusion barriers for Pathway 1 to 4 are 0.50 eV, 0.41 eV, 0.39 eV and 7.74 eV, which are in excellent agreement with our DFT calculated values.

3.3 QRNN Diffusivity

As described in section 2, we carried out large scale MD simulations to explore Li diffusion at different stages, Li contents and temperatures. Figure S7 shows the Li diffusivity (D) versus temperature (T) for all the 23 Li_xC_6 structures considered in this work. We find that D versus T of each structure can be represented by a single linear Arrhenius relation, therefore the 300 K D can be extrapolated from the D values at high temperatures. To verify this, we directly calculated the 300 K D values from 70 ns MD trajectories. In Figure 5a, we plot the extrapolated 300 K D values at different Li contents x and stages. The directly calculated 300 K D are shown by open markers. It should be pointed out that most directly calculated 300 K D exhibit large statistical uncertainty as the slop of MSD-dt is close to zero, such as the MSD-dt curve of $Li_{0.4}C_6$ in Figure S8b, therefore we only present
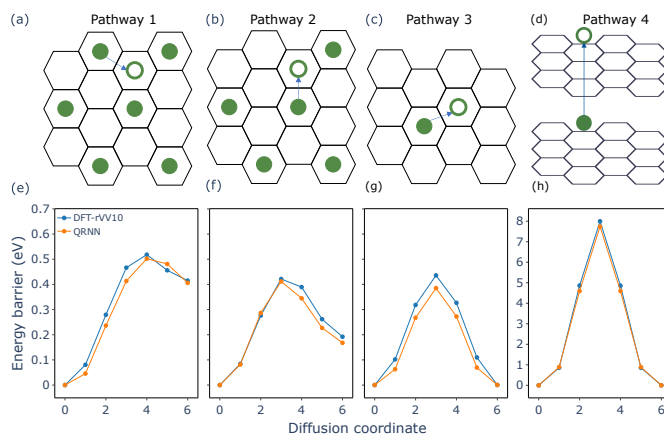

Fig. 4 The schematic figures illustrate the intralayer Li diffusion pathways from one site to a vacancy site, where there are two neighboring Li sites (a), one neighboring Li site (b) and no neighboring Li site (c). (d) shows interlayer pathways, where Li diffuses through a carbon hexagon. (e-h) depict the corresponding diffusion barriers calculated by rVV10 and QRNN.

the 300 K D values with low statistical uncertainty, such as the MSD-dt curve of $Li_{0.64}C_6$ in Figure S8a. We found that the directly calculated 300 K D values are close to the ones that are extrapolated from the diffusivities at high temperatures. Overall, we found a non-monotonic trend between D and x, with three pronounced minima at x=0.138, 0.247, and 0.493, where the Li_xC_6 structures undergo the phase transitions between different stages. In Figure 5b, we plot the Li occupation percentage in the unfilled Li layer with Li vacancies. It should be noted that when Li ions are removed from fully occupied Li layer, more Li ions diffuse with Pathway 2 and 3 which leads to a higher D because Li diffusion barriers of Pathway 2 and 3 are smaller than that of Pathway 1 (see Figure 4). However, a further Li ion removal from the unfilled Li layer leads to a smaller number of Li ions that diffuse with Pathway 2 and 3, and Li diffusion is dominated by Pathway 1 from the Li ions in the fully occupied Li layers, leading to a lower D. Both the minimum and maximum Li occupations in Figure 5 indicate the dominant Li diffusion with Pathway 1. This explains the initial increase and then decrease of D at $0.138 \leq x \leq 0.247$ and $0.4 \leq x \leq 0.493$. The local minima of D at x=0.4, 0.644, and 0.911 coincide with the regions where the two-phase regions are formed. The decrease of D can also be attributed to the dominant Li diffusion with Pathway 1. Using first-principles calculations and Monte Carlo simulations, Persson et al. also reported a non-monotonic relation between D and x in Li_xC_6 system with a sharp decrease in D at x=0.5, where stage 1 phase transits to stage 2 phase. [3] Here, we demonstrate that similar sharp decrease in D happens at other phase transition regions. The interaction between D and phase transition in Li_xC_6 system has also been demonstrated experimentally. Using the GITT technique, Park et al. reported a decrease in D at x=0.17, 0.25, and 0.5, with the formation of stage 4 LiC_{36}, stage 3 LiC_{24}, and stage 2 LiC_{12}, respectively. [15] Using the potentiostatic intermittent titration technique (PITT) and electrochemical impedance spectroscopy (EIS), Levi et al. also found a non-monotonic relation between D and x, with three pronounced minima that are related to phase transition be-
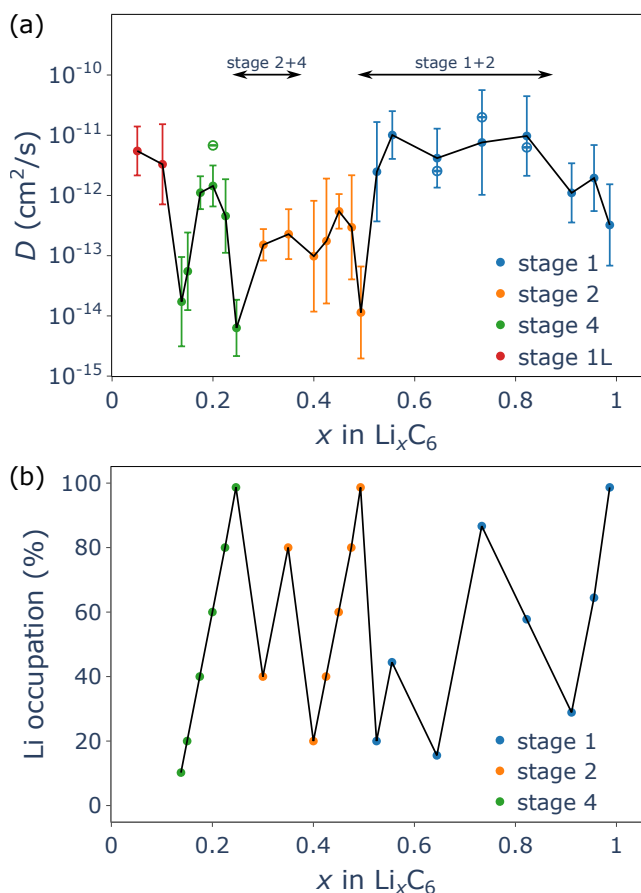
Fig. 5 (a) Calculated Li diffusivity (D) at 300 K as a function of Li content in Li_xC_6 system. Each D value at 300 K was extrapolated from the D values at higher temperatures using an Arrhenius relation. The error bars illustrate the uncertainty of this extrapolation. The open markers represent the D values that are directly calculated from the 70 ns MD trajectories at 300 K. (b) Li occupation percentage in the unfilled Li layer of the Li_xC_6 structures.

tween different stages.[37] On the other hand, using AC impedance method, the D versus x curve reported in Piao et al's work does not exhibit the phase transition induced diffusivity drop character.[16] Instead, the D value decreases significantly at $0 < x < 0.5$ from 10^{-9} to 10^{-11} cm^2/s. Interestingly, in Park et al's work, an opposite trend was observed, with D increasing from 10^{-11} to 10^{-10} cm^2/s at $0 < x < 0.5$.[15] Moreover, experimental data of D in graphite is also inconsistent and spans 10^{-6} to 10^{-16} cm^2/s [11–14]. Apart from different measuring methods, particle size and shape of the graphite electrode[38] as well as its surface area in contact with the electrolyte solution could all contribute to the inconsistent D values [11,14]. Though our calculated D values are within this range, it is difficult to compare the absolute values of each.

4 Conclusions

Using first-principles calculations, we studied the structural, energetic, and electrochemical properties of Li_xC_6 system. Comparing to the PBE functionals and previously reported *ab initio* results, the rVV10 functional accurately reproduces the experimental lattice parameters, phase stability, and voltage curve of the Li_xC_6 system. By implementing an active learning approach to sam-

ple additional Li_xC_6 structures and label them with the rVV10 functional, we developed an accurate and stable QRNN model for molecular dynamics simulations of the Li_xC_6 system. By carrying out large scale MD simulations, we investigated Li diffusion in Li_xC_6 structures as a function of stage, Li content and temperature. We found a non-monotonic trend between D and x, with three pronounced minima, where the Li_xC_6 structures undergo the phase transitions between different stages. The decrease of D near phase transition can be attributed to a decrease of fast diffusion Li ions. The phase transition dependent Li diffusion agrees well with previous experimental and theoretical results, demonstrating the capability of our QRNN model in unraveling the complex relation between Li diffusion and phase transition in a graphite anode. In addition, one rational approach to mitigate the phase transition induced Li diffusion bottleneck could be introducing porous structures in graphite which provides multi-channel Li diffusion.[39] Recently, Inamoto *et al.* reported that the Li diffusivity in the graphite structures with pores formed in the graphene is orders of magnitude higher than that of pristine graphite structures.[14]

Conflicts of interest

There are no conflicts of interest to declare.

Acknowledgements

Notes and references

1 J. Asenbauer, T. Eisenmann, M. Kuenzel, A. Kazzazi, Z. Chen and D. Bresser, *Sustainable Energy & Fuels*, 2020, **4**, 5387–5416.

2 Y. Liu, H. Shi and Z. S. Wu, *Energy & Environmental Science*, 2023, **16**, 4834–4871.

3 K. Persson, Y. Hinuma, Y. S. Meng, A. Van Der Ven and G. Ceder, *Physical Review B - Condensed Matter and Materials Physics*, 2010, **82**, 125416.

4 U. Hofmann and W. Rüdorff, *Transactions of the Faraday Society*, 1938, **34**, 1017–1021.

5 N. Daumas and A. Hérold, *CR Acad. Sci. Ser. C*, 1969, **268**, 373–375.

6 W. Zhou and P. H.-L. Sit, *ACS Omega*, 2020, **5**, 18289–18300.

7 C. Sole, N. E. Drewett and L. J. Hardwick, *Faraday Discussions*, 2014, **172**, 223–237.

8 A. M. Dimiev, G. Ceriotti, N. Behabtu, D. Zakhidov, M. Pasquali, R. Saito and J. M. Tour, *ACS Nano*, 2013, **7**, 2773–2780.

9 Y. Guo, R. B. Smith, Z. Yu, D. K. Efetov, J. Wang, P. Kim, M. Z. Bazant and L. E. Brus, *The Journal of Physical Chemistry Letters*, 2016, **7**, 2151–2156.

10 M. Heß and P. Novák, *Electrochimica Acta*, 2013, **106**, 149–158.

11 N. Takami, A. Satoh, M. Hara and T. Ohsaki, *Journal of The Electrochemical Society*, 1995, **142**, 371–379.

12 H. Yang, H. J. Bang and J. Prakash, *Journal of The Electrochemical Society*, 2004, **151**, A1247.

13 P. Yu, B. N. Popov, J. A. Ritter and R. E. White, *Journal of The Electrochemical Society*, 1999, **146**, 8–14.

14 J. Inamoto, S. Komiyama, S. Uchida, A. Inoo and Y. Matsuo, *Journal of Physical Chemistry C*, 2022, **126**, 16100–16108.

15 J. H. Park, H. Yoon, Y. Cho and C. Y. Yoo, *Materials*, 2021, **14**, 4683.

16 T. Piao, S. Park, C. Doh and S. Moon, *Journal of The Electrochemical Society*, 1999, **146**, 2794–2798.

17 K. Persson, V. A. Sethuraman, L. J. Hardwick, Y. Hinuma, Y. S. Meng, A. Van Der Ven, V. Srinivasan, R. Kostecki and G. Ceder, *Journal of Physical Chemistry Letters*, 2010, **1**, 1176–1180.

18 L. D. Jacobson, J. M. Stevenson, F. Ramezanghorbani, D. Ghoreishi, K. Leswing, E. D. Harder and R. Abel, *Journal of Chemical Theory and Computation*, 2022, **18**, 2354–2366.

19 S. Dajnowicz, G. Agarwal, J. M. Stevenson, L. D. Jacobson, F. Ramezanghorbani, K. Leswing, R. A. Friesner, M. D. Halls and R. Abel, *Journal of Physical Chemistry B*, 2022, **126**, 6271–6280.

20 P. Giannozzi, S. Baroni, N. Bonini, M. Calandra, R. Car, C. Cavazzoni, D. Ceresoli, G. L. Chiarotti, M. Cococcioni, I. Dabo, A. D. Corso, S. d. Gironcoli, S. Fabris, G. Fratesi, R. Gebauer, U. Gerstmann, C. Gougoussis, A. Kokalj, M. Lazzeri, L. Martin-Samos, N. Marzari, F. Mauri, R. Mazzarello, S. Paolini, A. Pasquarello, L. Paulatto, C. Sbraccia, S. Scandolo, G. Sclauzero, A. P. Seitsonen, A. Smogunov, P. Umari and R. M. Wentzcovitch, *Journal of Physics: Condensed Matter*, 2009, **21**, 395502.

21 D. Vanderbilt, *Physical Review B*, 1990, **41**, 7892–7895.

22 H. Rydberg, *Physical Review Letters*, 2003, **91**, year.

23 G. Henkelman, B. P. Uberuaga and H. Jónsson, *The Journal of Chemical Physics*, 2000, **113**, 9901–9904.

24 S. Grimme, C. Bannwarth and P. Shushkov, *Journal of Chemical Theory and Computation*, 2017, **13**, 1989–2009.

25 A. H. Larsen, J. J. Mortensen, J. Blomqvist, I. E. Castelli, R. Christensen, M. Dułak, J. Friis, M. N. Groves, B. Hammer, C. Hargus, E. D. Hermes, P. C. Jennings, P. B. Jensen, J. Kermode, J. R. Kitchin, E. L. Kolsbjerg, J. Kubal, K. Kaasbjerg, S. Lysgaard, J. B. Maronsson, T. Maxson, T. Olsen, L. Pastewka, A. Peterson, C. Rostgaard, J. Schiøtz, O. Schütt, M. Strange, K. S. Thygesen, T. Vegge, L. Vilhelmsen, M. Walter, Z. Zeng and K. W. Jacobsen, *Journal of Physics: Condensed Matter*, 2017, **29**, 273002.

26 K. J. Bowers, D. E. Chow, H. Xu, R. O. Dror, M. P. Eastwood, B. A. Gregersen, J. L. Klepeis, I. Kolossvary, M. A. Moraes, F. D. Sacerdoti, J. K. Salmon, Y. Shan and D. E. Shaw, SC '06: Proceedings of the 2006 ACM/IEEE Conference on Supercomputing, 2006, pp. 43–43.

27 J. Behler and M. Parrinello, *Physical Review Letters*, 2007, **98**, 146401.

28 S. Grimme, *Journal of Computational Chemistry*, 2006, **27**, 1787–1799.

29 J. Cheng, K. D. Fong and K. A. Persson, *Journal of Materials Chemistry A*, 2022, **10**, 22245–22256.

30 B. Vadlamani, K. An, M. Jagannathan and K. S. R. Chandran, *Journal of The Electrochemical Society*, 2014, **161**, A1731.

31 O. Lenchuk, P. Adelhelm and D. Mollenhauer, *Journal of Computational Chemistry*, 2019, **40**, 2400–2412.

32 T. Hu, J. Tian, F. Dai, X. Wang, R. Wen and S. Xu, *Journal of the American Chemical Society*, 2023, **145**, 1327–1333.

33 P. Y. Yang, Y. H. Chiang, C. W. Pao and C. C. Chang, *Journal of Chemical Theory and Computation*, 2023, **19**, 4533–4545.

34 Z. Chen, Y. Qin, Y. Ren, W. Lu, C. Orendorff, E. P. Roth and K. Amine, *Energy & Environmental Science*, 2011, **4**, 4023–4030.

35 J. R. Dahn, *Physical Review B*, 1991, **44**, 9170–9177.

36 S. Thinius, M. M. Islam, P. Heitjans and T. Bredow, *Journal of Physical Chemistry C*, 2014, **118**, 2273–2280.

37 M. D. Levi and D. Aurbach, *Journal of Physical Chemistry B*, 1997, **101**, 4641–4647.

38 C. Deng and W. Lu, *Journal of Power Sources*, 2020, **473**, 228613.

39 Q. Cheng, R. Yuge, K. Nakahara, N. Tamura and S. Miyamoto, *Journal of Power Sources*, 2015, **284**, 258–263.